15th International Symposium on Particle Image Velocimetry – ISPIV 2023
June 19–21, 2023, San Diego, California, USA

Multi-sheet illumination and consecutive overlapping 2D-2C PIV acquisition for enhanced access to boundary layer flows around obstructive opaque objects

S. Fu*, P. Suchandra*, S. Raayai-Ardakani†

Rowland Institute, Harvard University, Cambridge, MA, USA

* These authors contributed equally.

† Corresponding author: sraayai@fas.harvard.edu

Abstract

In experiments based on laser-diagnostic techniques, the field of view of the imaging can present limitations in the size of the flow area that can be investigated as well as the resolution of the acquisition. This is especially pertinent to external flows past objects where both the information in the boundary layer and the far field are important in understanding the physics of the problem. In this work, we introduce a variation in the experimental technique using a single laser and multiple light sheets with one camera, to perform high-resolution 2D-2C PIV measurements of relatively large opaque samples and areas of interest (compared with the available field of view of the camera). Here we focus on single-body, opaque samples such as hydrofoils, and multi-body samples with members arranged at structured distances from each other (suspended and fixed in the water from above). This experimental procedure aims to provide a baseline method to study the boundary layers and flows over the entirety of samples with complicated geometries and arrangements and provide statistical data for the theoretical and numerical modeling of such flows.

1 Introduction

External flows past objects comprise a substantial portion of the flows of interest to industrial applications and fluid mechanics. The introduction of laser diagnostic techniques, especially particle image velocimetry (PIV) (Adrian and Westerweel, 2011) has greatly expanded our experimental ability to study and assess the performance of such flows with much more details than other localized techniques. The resulting field data collected in such measurements are crucial for developing better theoretical and numerical models for flows, especially in high Reynolds numbers involving complex geometric boundaries.

However, the extent of data collected within one PIV experiment can be constrained due to different physical limitations. For example, the field of view of the camera and magnification used in the imaging (Michálek et al., 2022) dictate the extent of the flow region captured during the experiments to either high-resolution views of a small region (Abu Rowin and Ghaemi, 2019), or lower resolution images of a wider area (Terra et al., 2016). In addition, most solid objects used in experiments are non-transparent and the option of index-matching is not always available. This commonly results in dark shadow areas (Kim et al., 2015; Du et al., 2022; Nair et al., 2023) in the captured images.

To alleviate these limitations in a 2D-2C PIV, here we present a variation of the experimental technique to gain access to high-resolution information both in near- and far-field of an external flow past a single or arrays of non-transparent samples, without any shadow effects in difficult to reach areas. We design these experiments in a cost-effective manner with a single laser source and a single camera as opposed to multi-illumination/multi-camera setups (Parikh et al., 2023) used to access large fields of views. We introduce a few optical elements, specifically beam splitters, to create multiple light sheets simultaneously illuminating the experimental area from various directions and use a Computer Numerically Controlled (CNC) stage to maneuver the camera within the experimental area of interest.

Here, we present the steps of implementing this procedure to study the boundary layers on both sides of a slender plate as well as the details of the flow in the interior of arrays of cylinders in the flow. As for boundary layers, previous experimental approaches have focused on partial locations within the length of the plate (Grek et al., 1996; Xu et al., 2021), or single side measurements (Abu Rowin and Ghaemi, 2019; Grek et al., 1996). Experimental studies of non-transparent arrays on the other hand are mainly focused on the wake or the exterior of the arrangements (Ricardo et al., 2016; Kazemi et al., 2018; Gymnopoulos et al., 2019; Kazemi et al., 2021; Ferreira et al., 2021; Yagci et al., 2021; Nair et al., 2023) with internal details mostly available from numerical models (Chang and Constantinescu, 2015; Tang et al., 2020; Liu et al., 2021; Nair et al., 2023).

2 Experimental setup

The experiments are conducted in a water tunnel facility with an active cross-sectional area of 0.2×0.2 m^2, and a length of 2 m (Fig. 1), at a free-stream velocity of 0.185 m/s (turbulence intensity of less than 1% in the free-stream). Samples of interest are suspended in the tunnel from the top of the tunnel and are fixed to the top edge of the tunnel, placed at a distance of about $70-75$ cm from the tunnel entrance. For a single sample case, we use a thin plate with the leading edge streamlined into an elliptical shape as discussed by Fu and Raayai-Ardakani (2023). As for the multi-object case, 5 cylinders with diameters of $d = 6$ mm are placed in a V-shaped formation with streamwise spacings of $2.5d$, and point angles of 37°.

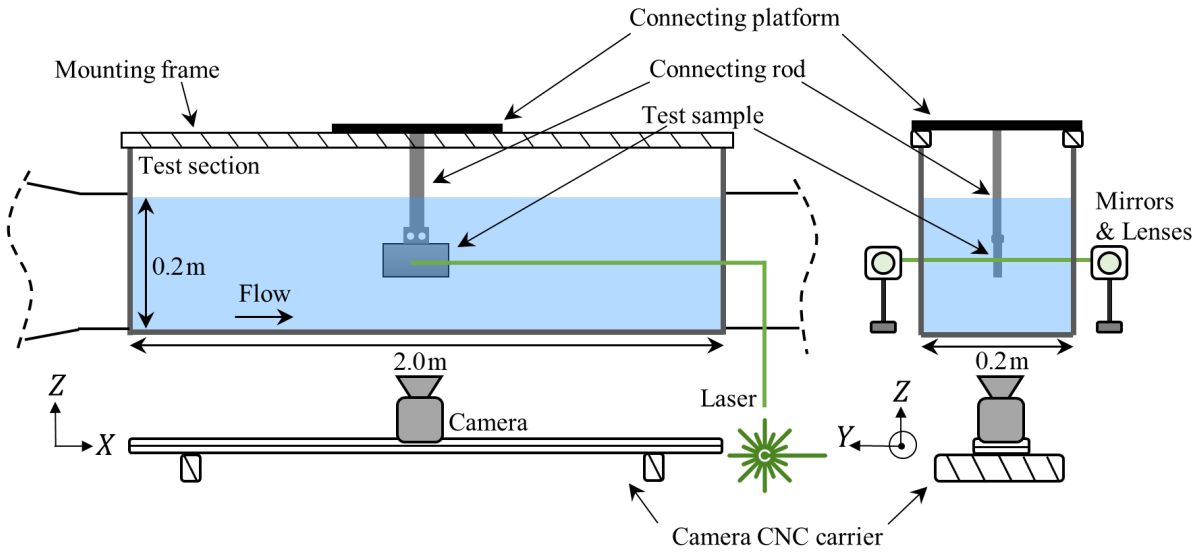

Figure 1: Schematic of the experimental water tunnel facility and the PIV components (front view and side view). The global coordinate system, shown as (X, Y, Z), is used during the experimental procedure to control the location of the sample and camera.

The measurements are conducted using a 2D-2C PIV procedure, with a double-pulsed Nd:YAG laser at 15 Hz repetition rate (Evergreen EVG00200, Quantel Laser), a high-speed camera (Chronos 2.1, Kron Technologies Inc.) at a resolution of 720×1920 pixels with a 100 mm macro lens (Canon EF 100mm f/2.8L Macro Lens), and an Arduino Teensy Board programmed to serve as a timing unit to synchronize the laser shots and the camera captures (Teensy Timer Tool, 2023). The timing between the two consecutive pulses is set at 1000 μs. The water is seeded with 10 μm hollow glass particles (TSI incorporated). As seen in Fig. 1, the camera is attached to a 3-axis CNC motorized stage and is located underneath the tunnel. More details have been discussed by Fu and Raayai-Ardakani (2023).

2.1 Accessing shadows and multi-body obstructions

The first challenge to consider here is the case of shadow(s) created by the body of the object in a single sample experiment. To avoid this shadow, and have simultaneous access to both sides of the sample, we introduce a half-wave-plate (HWP, see tutorial (Half-Wave-Plate, 2023)) and a polarizing beam splitter (PBS, see selection guide (Polarizing-Beam-Splitter, 2023)) to divide the incoming linearly polarized beam of the laser into two nearly equal beams and guide the two beams with additional mirrors toward the area of interest on either side of the sample. From there, two identical light sheet optics (a combination of two spherical (L Sph) and one cylindrical (L Cyl) lenses) are used on the two opposite sides of the water tunnel. This double-light sheet strategy (as shown in Fig. 2(a)) thus illuminates both sides of the sample and in the absence of the sample, the two would meet each other to create a sheet with nearly double the illumination intensity. Note that instead of combinations of wave-plates and polarizing beam splitters, non-polarizing beam splitters (see selection guide (Beam-Splitter, 2023)) can be used for low-energy lasers.

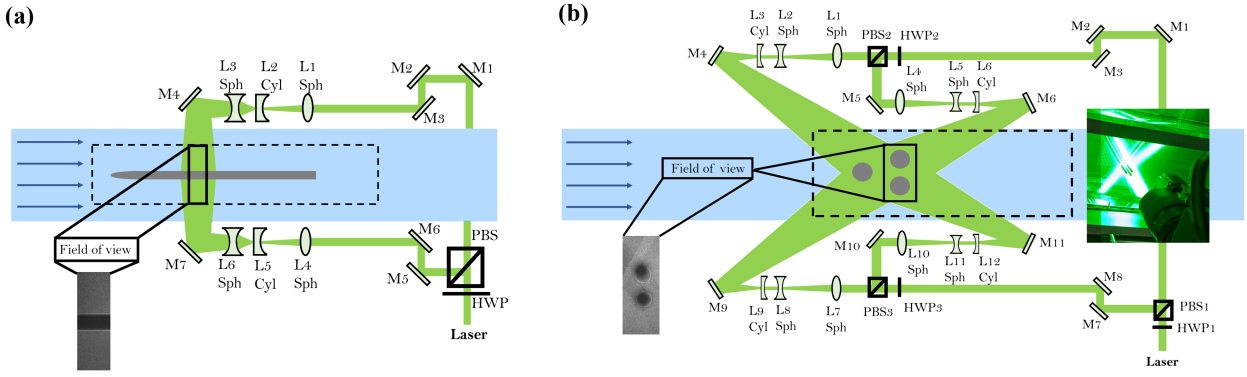

Figure 2: Schematic of multiple-sheet illumination strategies: (a) Double-sheet setup for simultaneous illumination of two sides of an opaque sample (Fu and Raayai-Ardakani, 2023). (b) Quadruple-sheet for visualizing the flow in the interior of a multi-member sample, which would still be in shadow if double-sheet is used. The view of the intersection of the four light sheets around the members of the sample array is also shown from the bottom of the tunnel. In both cases, the field of view of the camera (solid lines) is smaller than the total area of interest which is marked by dashed lines.

In multi-body samples, the distribution of the dark spots within the field of view of the camera is more complicated, and in most scenarios, even a double-light-sheet strategy demonstrated above will not be sufficient to illuminate the entire periphery of the sample leading to dark spot(s) between the various members. Thus, for this case, we employ a quadruple-sheet lighting strategy at various angles to allow the light to reach the flow field in the interior of the sample arrangement. For this, we keep the initial HWP, PBS, and mirrors to bring the two light beams to the front and back side of the tunnel, and afterward, by introducing two additional HWP and PBS pairs, the four light beams are directed to four identical lens combinations to create the four separate light sheets (Fig. 2(b)). For the regions exterior to the multi-body sample and the regions upstream and downstream of the sample, a double-light sheet is sufficient and used here.

However, even with the quad-sheet illumination, increasing the number of obstacles, can at times increase the area or the number of dark spots visible between the various members. In such cases, with a slight change in the angle of the light sheet, we can illuminate the previously dark area while placing a different location in shadow (Fig. 3). Therefore, to address this challenge, we image the field of view more than once with varying angles of laser sheets so that each portion of the field of view is illuminated (without shadow) in at least one of the images as shown in the two variations in Fig. 3(b).

For single samples with a double-light sheet strategy, the laser is operated at nominal pulse energies of $20-30$ mJ per pulse which is divided into two beams of about $10-15$ mJ per pulse in either sheet. For multi-sample, quad-sheet cases, the laser is operated at a higher pulse energy of $40-60$ mJ per pulse that leads to pulse energies of about $10-15$ mJ per pulse in each of the sheets.

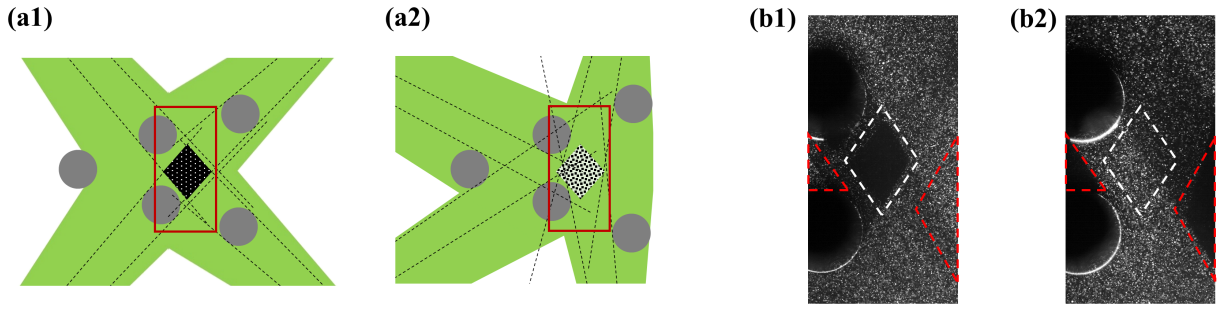

Figure 3: (a) Schematic of a field of view illuminated with two different quad-sheet setups from different angles. By moving the light sheets from configuration (a1) to configuration (a2) we can illuminate a previously dark area (black area in (a1) and patterned area in (a2)). (b) Images of a field of view captured with two quad-sheets at different angles resulting in two different variations of dark spots, the white-marked spot in (b1) and the red-marked spots in (b2). The experiments can be performed with (b1) first to capture the information in the red-marked spots, missing the information in the white-marked area, and then change to (b2) to capture the flow in the white-marked spot, missing the flow information in the red-marked spots. As it is clear the order of these two experiments does not matter.

2.2 Imaging of large areas of interest

The second challenge in the acquisition of high-resolution data over a large area of interest is related to the limits in the field of view of the camera. Especially, the high resolution and magnification of the measurements limit the field of view of the imaging to only a portion of the experimental area (Figs. 2 and 4). Therefore, to access the entire view, we repeat the experimental procedure in overlapping, consecutive steps by systematically moving the camera via the CNC stage and manual adjustments in the light-sheet optics. For small or slender enough samples, a one-dimensional camera sweep (Fig. 4(a)) is sufficient to be able to capture the details of the boundary layer and the inviscid flow (Fu and Raayai-Ardakani, 2023). However, for larger and multi-body samples, a two-dimensional (Fig. 4(b)) sweep is required to be able to image the flow field and the wake behind the samples. Two examples of 1D and 2D camera sweeps used to image a thin plate and a multi-body sample with 3 cylinders in the flow are shown in Fig. 4. The 1D sweep has overlaps of about $40-45\%$ and the 2D sweep uses about 30% overlap in the streamwise direction and about $20-50\%$ overlap in the normal direction as deemed fit depending on the number of array members. For the 5-member case whose results are discussed in the next section, the overlap in the normal direction is 48%. In post-processing and analysis, we use the global location of the camera at each step (Fig. 1) and the physical size of the pixels and stitch the images together to get the full view of the sample.

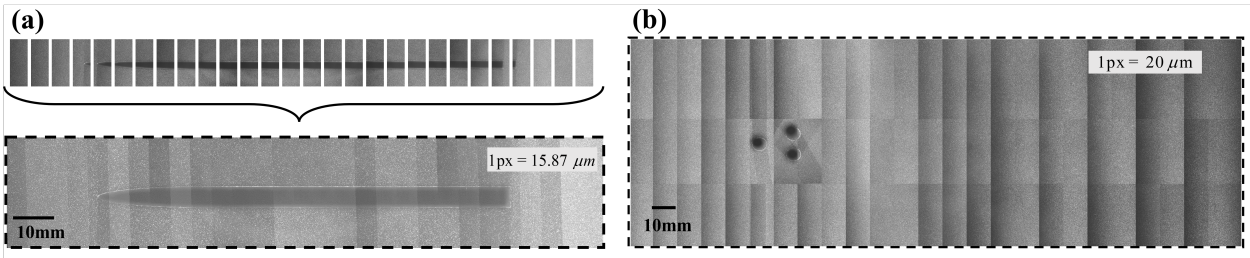

Figure 4: (a) Snapshots of a series of images acquired using the consecutive-overlapping technique in a 1D sweep covering the entire length of the sample as well as before and after the sample, and the fully stitched view of the images showing the full view of the sample (Fu and Raayai-Ardakani, 2023) (b) Fully stitched view of a series of overlapping images captured using a 2D sweep for flow past 3 cylinders.

3 Results

Using the procedure described earlier, here we present the results of two example experiments for a slender plate with double-sheet lighting, and an array of 5-members with quad-sheet lighting. In this 5-member case, even with the quad-sheets, the obstructions due to the four trailing members lead to a slight shadow remaining (similar to the schematic in Fig. 3(a)) which is then imaged twice with light sheets at different angles in the manner discussed earlier in Sec. 2.1 and Fig. 3. For slender plates, a total of 50 image pairs, and for the 5-member case a total of 100 image pairs have been used (sufficient statistically).

The PIV images are processed using the open-source software OpenPIV (Liberzon et al., 2020) with 32×32 windows and a search area of 64×64 with 85% overlap. In addition, for the case of slender plates, to avoid bias errors in the boundary layers close to the walls (Kähler et al., 2012) and to reduce the averaging effect of the square windows, the first 64 pixels in the near-wall region are analyzed with an in-house cross-correlation scheme with a rectangular window of 32×16 (smaller height in the normal direction) (Fu and Raayai-Ardakani, 2023).

As an example, Fig. 5(a) shows the vorticity field (normalized by an average shear rate $\dot{\gamma} = U_\infty/\delta = (U_\infty/L)\sqrt{\mathrm{Re}_L}$) in the boundary layer past a slender plate and the separated shear layers in the trailing edge of the sample at a global Reynolds number of $\mathrm{Re}_L = \rho U_\infty L/\mu = 18,500$. The figure clearly shows that by using consecutive-overlapping imaging, we are able to capture the details of the flow in near- and far-field as well as in the leading and trailing edge areas.

In addition, we can extract the velocity distribution in the boundary layers on either side, and one example is shown in Fig. 5(b). The velocity in the x direction, normalized by the maximum velocity of the cross-section ($U(x)$) is presented in terms of the similarity variables of the best Falker-Skan fits (Kundu et al., 2015), $\eta = y/x\sqrt{\mathrm{Re}_x(m/2)}$, for both front ($m = -0.0156$, $\mathrm{Re}_x = 12189.8$) and back ($m = 0.0167$, $\mathrm{Re}_x = 12169.3$) sides ($\mathrm{Re}_x = \rho U(x)x/\mu$ is the local Reynolds number). The two profiles show a slight difference in the performance of the two sides; The back side is more attached ($m > 0$) and the front side is slightly detached ($m < 0$) compared to the Blasius solution. As it can be seen, access to both sides of the sample using the double-light sheet allows us to capture this trend, and more explanation on the physics behind this is discussed by Fu and Raayai-Ardakani (2023).

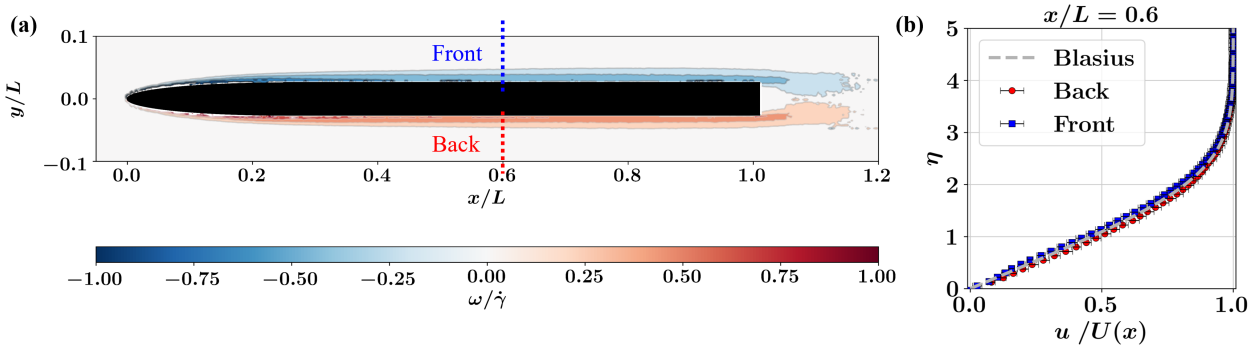

Figure 5: (a) Contours of vorticity non-dimensionalized by $\dot{\gamma} = (U_\infty/L)\sqrt{\mathrm{Re}_L}$, in a boundary layer past a slender plate at $\mathrm{Re}_L = 18,500$. (b) Velocity profiles on the front and back sides of the sample at $x/L = 0.6$ as marked in part (a). Velocities are non-dimensionalized with the maximum velocity at the cross-section, resulting in a local Reynolds number of $\mathrm{Re}_x = 12189.8$ ($m = -0.0156$), and $\mathrm{Re}_x = 12169.3$ ($m = 0.0167$) on the front and back respectively, and plotted as a function of the similarity variable η. Error bars represent the 95% confidence intervals. Additional information is discussed by Fu and Raayai-Ardakani (2023).

Similarly, we have access to the velocity profiles all along the length on either side of the sample and this detailed access allows us to also calculate the local shear stress distribution along both sides and thus be able to calculate the total drag force (Fu and Raayai-Ardakani, 2023). As an example, for the slender sample, the local skin friction coefficient at $x/L = 0.6$ (shown in Fig. 5(b)) on the front and back sides of the sample is found to be around 0.0054 and 0.0066 respectively.

Fig. 6 shows the contours of streamwise velocity in flow past an array of 5 members where again the consecutive-overlapping imaging performed in the form of a 2D sweep allows us to capture details of a large area of interest and the quad-light sheets allow us to get access to the details of the mean flow in the interior of the array. As a result, we can also extract local velocity profiles at different cross-sections of the flow,

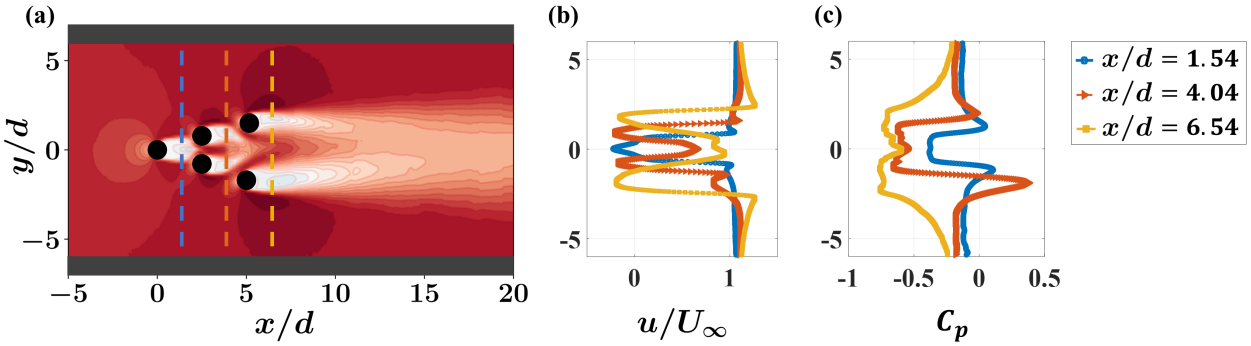

Figure 6: (a) Contours of streamwise velocity, normalized by the free-stream velocity in flow past a 5-member array at $\mathrm{Re}_d = \rho U_\infty d/\mu = 1100$. (b) Profiles of normalized streamwise velocity at three different cross-sections as marked in part (a). (c) Normalized pressure distribution, presented in terms of the pressure coefficient $C_p = (p - p_\infty)/(0.5\rho U_\infty^2)$, at three different locations corresponding to the profiles in part (b) and marked in part (a).

and three examples are shown in Fig. 6(b). We also use the velocity distribution and calculate the pressure distribution using directional integrals of the Navier-Stokes equations (Charonko et al., 2010) (similar to the procedure described by Fu and Raayai-Ardakani (2023)) and the pressure distribution is shown in Fig. 6(c). The velocity and pressure distributions can be used to calculate drag forces on the array members.

As it can be seen in Fig. 6(a), complex interactions exist between the wakes of different cylinders. The rear cylinders block the full development of the wake(s) of the cylinder(s) in front of them causing the wakes to bend inwards. The local velocity profiles shown in Fig. 6(b) exhibit multiple slow-downs: the larger slow-downs are due to the velocity deficits from the wakes of the upstream cylinders, and the smaller slow-downs are due to the upcoming stagnation points on the downstream cylinders. The corresponding pressure coefficient profiles in Fig. 6(c) exhibit pressure loss in most of the wake region due to the velocity deficit, and pressure gain is observed where the flow approaches the upcoming stagnation points.

4 Conclusions

Here, we present a variation of the 2D-2C PIV with multiple light sheets and consecutive overlapping imaging using a single laser and camera. By introducing half-wave-plates and polarizing beam splitters, a high-energy laser pulse is divided into multiple beams and directed to illuminate dark shadows and hard-to-reach areas of the sample. A CNC motorized stage is employed to repeat the imaging all over the experimental area of interest which is larger than the field of view of the camera. Then, the acquired images are stitched together to analyze the result and calculate the velocity field around the samples.

Ultimately, we present a few examples of results from experiments conducted using a slender plate and multi-cylinder samples to demonstrate the capability of this technique. As it is seen from the two cases, the multi-light sheet strategies offer an effective way of accessing the entire periphery of samples or the interior of multi-object setups and allow us to be able to study the details of the flow without any omissions. Consecutive-overlapping imaging, either 1D or 2D sweeps then enables us to gather the flow information over an experimental area larger than the field of view of the camera at a higher resolution than what is possible with a single camera. Either or both of the steps introduced here can be implemented in a variety of 2D-2C PIV settings and effectively used for studies of samples with complex boundaries in external flow conditions.

Acknowledgements

This work is supported by the Rowland Fellows program at Harvard University. The design and assembly of this experimental setup have been through multiple iterations and the details presented here are those of the most recent version. The authors thank Lars Caspersen, Mayesha Soshi, Dr. Yeonsu Jung, Richard Christopher Stokes, and Prof. Leah Mendelson for their assistance and discussions at various stages of this development.

References

Abu Rowin W and Ghaemi S (2019) Streamwise and spanwise slip over a superhydrophobic surface. *Journal of Fluid Mechanics* 870:1127–1157

Adrian RJ and Westerweel J (2011) *Particle image velocimetry*. Cambridge University Press

Beam-Splitter (2023) Beam splitter selection guide. https://www.thorlabs.com/newgrouppage9.cfm?objectgroup_id=754. Accessed: 2023-05-09

Chang K and Constantinescu G (2015) Numerical investigation of flow and turbulence structure through and around a circular array of rigid cylinders. *Journal of Fluid Mechanics* 776:161–199

Charonko JJ, King CV, Smith BL, and Vlachos PP (2010) Assessment of pressure field calculations from particle image velocimetry measurements. *Measurement Science and Technology* 21:1–15

Du Z, Li H, Cao Y, Wan X, Xiang Y, Lv P, and Duan H (2022) Control of flow separation using biomimetic shark scales with fixed tilt angles. *Experiments in Fluids* 63:158

Ferreira RML, Gymnopoulos M, Prinos P, Alves E, and Ricardo AM (2021) Drag on a square-cylinder array placed in the mixing layer of a compound channel. *Water* 13:1–23

Fu S and Raayai-Ardakani S (2023) Double-light-sheet, consecutive-overlapping particle image velocimetry for the study of boundary layers past opaque objects. https://doi.org/10.48550/arXiv.2304.14513

Grek G, Kozlov V, and Titarenko S (1996) An experimental study of the influence of riblets on transition. *Journal of fluid mechanics* 315:31–49

Gymnopoulos M, Ricardo AM, Alves E, and Ferreira RML (2019) A circular cylinder in the main-channel/floodplain interface of a compound channel: effect of the shear flow on drag and lift. *Journal of Hydraulic Research* 58:420–433

Half-Wave-Plate (2023) Half wave plate tutorial. https://www.thorlabs.com/newgrouppage9.cfm?objectgroup_id=711. Accessed: 2023-05-09

Kähler CJ, Scharnowski S, and Cierpka C (2012) On the uncertainty of digital PIV and PTV near walls. *Experiments in fluids* 52:1641–1656

Kazemi A, Castillo L, and Curet OM (2021) Mangrove roots model suggest an optimal porosity to prevent erosion. *Scientific Reports* 11:1–14

Kazemi A, de Riet KV, and Curet OM (2018) Drag coefficient and flow structure downstream of mangrove root-type models through PIV and direct force measurements. *Physical Review Fluids* 3:1–20

Kim N, Kim H, and Park H (2015) An experimental study on the effects of rough hydrophobic surfaces on the flow around a circular cylinder. *Physics of Fluids* 27:085113

Kundu PK, Cohen IM, and Dowling DR (2015) *Fluid mechanics*. Academic press, Massachusetts. 5th edition

Liberzon A, Lasagna D, Aubert M, Bachant P, Käufer T, jakirkham, Vodenicharski B, Dallas C, Borg J, tomerast, and ranleu (2020) OpenPIV/openpiv-python: OpenPIV - Python an open source particle image velocimetry (ver. 0.22.0)

Liu M, Huai W, Ji B, and Han P (2021) Numerical study on the drag characteristics of rigid submerged vegetation patches. *Physics of Fluids* 33:1–19

Michálek P, Procházka P, Uruba V, and Pospíšil S (2022) Influence of surface roughness on the wake structure of a circular cylinder at Reynolds number 5×10^3 to 12×10^3. *European Journal of Mechanics-B/Fluids* 96:15–25

Nair A, Kazemi A, Curet O, and Verma S (2023) Porous cylinder arrays for optimal wake and drag characteristics. *Journal of Fluid Mechanics* 961:A18

Parikh A, Fuchs T, Bross M, and Kähler CJ (2023) LEGO calibration targets for large-FOV particle image velocimetry. *Experiments in Fluids* 64:34

Polarizing-Beam-Splitter (2023) Polarizing beam splitter selection guide. https://www.thorlabs.com/newgrouppage9.cfm?objectgroup_id=739. Accessed: 2023-05-09

Ricardo AM, Sanches PM, and Ferreira RML (2016) Vortex shedding and vorticity fluxes in the wake of cylinders within a random array. *Journal of Turbulence* 17:999–1014

Tang T, Yu P, Shan X, Li J, and Yu S (2020) On the transition behavior of laminar flow through and around a multi-cylinder array. *Physics of Fluids* 32:1–13

Teensy Timer Tool (2023) Double Exposure Laser Illuminator. https://github.com/luni64/TeensyTimerTool. Accessed: 2023-03-20

Terra W, Sciacchitano A, and Scarano F (2016) Drag analysis from PIV data in speed sports. *Procedia engineering* 147:50–55

Xu M, Yu N, Kim J et al. (2021) Superhydrophobic drag reduction in high-speed towing tank. *Journal of Fluid Mechanics* 908:A6

Yagci O, Karabay O, and Strom K (2021) Bleed flow structure in the wake region of finite array of cylinders acting as an alternative supporting structure for foundation. *Journal of Ocean Engineering and Marine Energy* 7:379–403